J. Fluid Mech. (2007), *vol.* 588, *pp.* 163–187.
doi:10.1017/S0022112007007392 Printed in the United Kingdom

Linear feedback control and estimation applied to instabilities in spatially developing boundary layers

MATTIAS CHEVALIER[1,2], JÉRÔME HŒPFFNER[2], ESPEN ÅKERVIK[2] AND DAN S. HENNINGSON[1,2]

[1]The Swedish Defence Research Agency (FOI), SE-164 90, Stockholm, Sweden

[2]Linné Flow Centre, KTH Mechanics, SE-100 44, Stockholm, Sweden

(Received 6 April 2006 and in revised form 14 May 2007)

This paper presents the application of feedback control to spatially developing boundary layers. It is the natural follow-up of Högberg & Henningson (*J. Fluid Mech.* vol. 470, 2002, p. 151), where exact knowledge of the entire flow state was assumed for the control. We apply recent developments in stochastic models for the external sources of disturbances that allow the efficient use of several wall measurements for estimation of the flow evolution: the two components of the skin friction and the pressure fluctuation at the wall. Perturbations to base flow profiles of the family of Falkner–Skan–Cooke boundary layers are estimated by use of wall measurements. The estimated state is in turn fed back for control in order to reduce the kinetic energy of the perturbations. The control actuation is achieved by means of unsteady blowing and suction at the wall. Flow perturbations are generated in the upstream region in the computational box and propagate in the boundary layer. Measurements are extracted downstream over a thin strip, followed by a second thin strip where the actuation is performed. It is shown that flow disturbances can be efficiently estimated and controlled in spatially evolving boundary layers for a wide range of base flows and disturbances.

1. Introduction

There is much to be gained in the application of control to fluid mechanical systems, the most widely recognized and targeted aim being the reduction of skin friction drag on airplane wings. Flow control is a growing field and much research effort has been put into in both fundamental understanding and direct application of control methods. For a review see e.g. Bewley (2001) and Högberg & Henningson (2002).

Linear control theory gives powerful model-based tools for application of control to fluid systems provided the system at hand can be described well by a linear dynamic model. The theory of linear–quadratic–Gaussian control (LQG) is one of the major achievements in the field of control theory. It gives a methodology to compute the optimal, measurement-based, control when the dynamic model is linear, the objective is quadratic, and the external sources of excitations are stochastic. This theory is applied to boundary layer control in the present work.

Feedback control design can be conceptually and technically decomposed into two subproblems. The first subproblem is to estimate the flow state from noisy wall measurements. In our case, the state is the flow perturbation about the known base

flow profile. The estimator is a simulation of the dynamic system that is run in parallel with the flow. Its state is forced by a feedback of the measurements in order to converge to the real flow state. The estimated state is in turn used for feedback control of the flow, which constitutes the second subproblem. The closed loop system with estimation and control is commonly referred to as measurement feedback control or compensator.

This paper is a follow-up of Högberg & Henningson (2002) in which full information control was applied to spatially developing flows. The use of stochastic models for external sources of excitation was introduced in Hœpffner *et al.* (2005) and Chevalier *et al.* (2006), which allows computation of well-behaved estimation feedback kernels for three wall measurements: the two components of the skin friction and the wall pressure. Each of these three measurements provides the estimator with additional information on the instantaneous flow state. This variety of measurements is useful when complex flows are targeted. This improvement of the estimation thus makes it possible to apply the full theory of feedback control to complex flow cases such as the transitional scenarios presented in this paper. For this reason, we have systematically reconsidered the flow cases of Högberg & Henningson (2002), where exact knowledge of the entire flow state was assumed, and applied measurement-feedback control, where the estimated flow state is used for control. We have compared the performance of the full information control of Högberg & Henningson (2002) and the present estimation based control, and found it satisfactory.

One of the major limitations to the application of control to spatially distributed systems (system, in space and time, usually described by partial differential equations) is the realization of the sensing and actuation that would handle relatively fast events as well as small scales of fluid motion. In addition, control over physical surfaces typically requires dense arrays of sensors and actuators. Recent development in MEMS technology and related research may lead to solutions of this problem. For application of MEMS technology to flow control see e.g. Yoshino, Suzuki & Kasagi (2003).

Several recent investigations have pursued the application of LQG-type feedback control to wall-bounded flow systems. A recent overview is given in Kim (2003). Högberg, Bewley & Henningson (2003*a*) demonstrated the localization of the feedback kernels. This property allows a local application of the control, i.e. only the local properties of the system (dynamics, disturbance sources and measurement information) are necessary for control. The efficiency of the control scheme we use here was illustrated in Högberg, Bewley & Henningson (2003*b*), where relaminarization of a fully developed turbulent flow was achieved. In Hœpffner *et al.* (2005) and Chevalier *et al.* (2006), the focus was on the estimation performance. By introducing a relevant model for the external source of disturbance, it was possible to improve the estimation performance for both transitional and turbulent flows.

The procedures of control design are based on the manipulations of a linear dynamic model for the flow system, which is typically of large order. In the case of spatially invariant systems, i.e. system for which the dynamics is independent of some spatial coordinates, the problem can be decoupled into a parameterized family of smaller systems. In our case, we assume spatial homogeneity over the two horizontal directions. After Fourier transforming, this allows us to design and tune the controller and estimator for individual wavenumber pairs.

In a spatially developing flow such as the boundary layer, this procedure can still be used, even though the spatial invariance in the streamwise direction is lost. The localization of the control and estimation kernels ensures that the feedback

is local, so that the flow can be assumed to be locally parallel. In Högberg & Henningson (2002), the actuation was successfully applied over a strip parallel to the leading edge in Falkner–Skan–Cooke (FSC) boundary layers, and the control feedback law was computed based upon the local Reynolds number. In Högberg, Chevalier & Henningson (2003*c*), a measurement strip was added, and the subsequent state estimate was used for control. The present paper aims to apply the recent development and improvement to the estimation of the complex flow cases where the full information control was shown to be successful in Högberg & Henningson (2002).

The structure of this paper is as follow. In § 2, the flow system is described: dynamics, input and output. In § 3, we outline the main issues for the feedback control and estimation. The numerical method is described in § 4. The performance of the control in several flow cases is shown in § 5, and concluding remarks are given in § 6.

2. System description

2.1. *Flow dynamics*

The Navier–Stokes equations are linearized about solutions of the FSC boundary layer. Favourable and adverse pressure gradients can be accounted for as well as the effect of a sweep. To obtain the family of FSC similarity solutions we assume that the chordwise outer-streamline velocity obeys the power law $U_\infty^* = U_0^*(x^*/x_0^*)^m$ and that the spanwise free-stream velocity W_∞^* is constant. U_0^* is the free-stream velocity at a fixed position x_0^*, the physical distance from the leading edge, and the asterisks ($*$) denote dimensional quantities. Note that the Blasius profile is a special case of the FSC boundary layer with zero crossflow component and no pressure gradient. If we choose the similarity variable ξ as

$$\xi(y^*) = y^* \sqrt{\frac{m+1}{2}\frac{U_\infty^*}{2\nu x^*}}$$

we can derive the following self-similar boundary layer profiles:

$$f''' + ff'' + \beta_h(1 - f'^2) = 0,$$
$$g'' + fg' = 0,$$

where the Hartree parameter β_h is related to the power-law exponent m by $\beta_h = 2m/(m+1)$. The accompanying boundary conditions are

$$f = f' = g = 0 \quad \text{for} \quad \xi = 0,$$
$$f' \to 1, \quad g \to 1 \quad \text{as} \quad \xi \to \infty.$$

The complete derivation can be found in e.g. Schlichting (1979) and Cooke (1950). From the FSC similarity solutions f and g, we construct the non-dimensional velocity profiles

$$U(y) = f'(\xi(y)), \qquad W(y) = \frac{W_\infty^*}{U_\infty^*} g(\xi(y)), \tag{2.1a, b}$$

for a fixed $x = (x^* - x_0^*)/\delta_0^*$ and where $y = y^*/\delta_0^*$. The symbol δ_0^* denotes the displacement thickness at position $x^* = x_0^*$. The velocity profiles (2.1*a*) and (2.1*b*) are then used as base flow when constructing the linear dynamic model for the flow disturbance and the initial conditions for the direct numerical simulations (DNS).

Once linearized, the system can be transformed to Fourier space by assuming local spatial invariance. This implies that the non-parallel effects are small, i.e. the base flow

is slowly developing in the streamwise direction. After transformation to the velocity–vorticity ($v-\eta$) formulation, we obtain the Orr–Sommerfeld/Squire equations (see e.g. Schmid & Henningson 2001)

$$\begin{pmatrix} \dot{v} \\ \dot{\eta} \end{pmatrix} = \begin{pmatrix} \mathscr{L}_{OS} & 0 \\ \mathscr{L}_{C} & \mathscr{L}_{SQ} \end{pmatrix} \begin{pmatrix} v \\ \eta \end{pmatrix}, \tag{2.2}$$

where

$$\left.\begin{aligned} \mathscr{L}_{OS} &= \Delta^{-1}[-\mathrm{i}(k_x U + k_z W)\Delta + \mathrm{i}k_x U'' + \mathrm{i}k_z W'' + \Delta^2/Re], \\ \mathscr{L}_{SQ} &= -\mathrm{i}(k_x U + k_z W) + \Delta/Re, \\ \mathscr{L}_{C} &= \mathrm{i}(k_x W' - k_z U'), \end{aligned}\right\} \tag{2.3}$$

and where the Laplacian operator is denoted $\Delta = \mathrm{D}^2 - k^2$ and D is the wall-normal derivative and $k^2 = k_x^2 + k_z^2$. The boundary conditions are defined as

$$\left.\begin{aligned} v(0,t) = \varphi, \quad \mathrm{D}v(0,t) = 0, \quad \eta(0,t) = 0, \\ v(y,t) = 0, \quad \mathrm{D}v(y,t) = 0, \quad \eta(y,t) = 0 \quad \text{as} \quad y \to \infty. \end{aligned}\right\} \tag{2.4}$$

The control actuation affects the system through a non-homogeneous boundary condition on the wall-normal velocity $\varphi(t)$ (time-varying wall blowing and suction). The Reynolds number Re is based on the free-stream velocity and displacement thickness.

In order to apply tools from control theory, see for example Lewis & Syrmos (1995), it is convenient to write the linearized fluid system in the general state-space form

$$\left.\begin{aligned} \dot{\boldsymbol{q}} &= \boldsymbol{A}\boldsymbol{q} + \boldsymbol{B}_2\boldsymbol{u}_c + \boldsymbol{B}_1\boldsymbol{f}, \quad \boldsymbol{q}(0) = \boldsymbol{q}_0, \\ \boldsymbol{y} &= \boldsymbol{C}\boldsymbol{q} + \boldsymbol{g}, \end{aligned}\right\} \tag{2.5}$$

where $\boldsymbol{q}$ is the state, and ($\boldsymbol{A}$) is the linear operator representing the dynamics of the system. The external disturbances, denoted by $\boldsymbol{f}$, force the state through the input operator $\boldsymbol{B}_1$, and $\boldsymbol{q}_0$ is the initial condition. The operator $\boldsymbol{B}_1$ transforms a forcing on (u, v, w) to a forcing on (v, η), since the flow state is expressed in this formulation. The control signal u_c affects the system through the input operator $\boldsymbol{B}_2$. Operator $\boldsymbol{C}$ extracts the measurements from the state variable, and $\boldsymbol{g}$ adds a stochastic measurement noise with given statistical properties. The noisy measurement is then denoted by $\boldsymbol{y}$.

The controlled Orr–Sommerfeld/Squire system can be cast into the formalism of (2.5) by means of a lifting procedure (see e.g. Högberg *et al.* 2003*a*) where the control at the wall now enters the flow through a volume forcing term instead of as an inhomogeneous boundary condition at the wall. This is done by decomposing the flow state into a time-varying homogeneous component (subscript h) and a steady particular (subscript p) component:

$$\begin{pmatrix} v(t) \\ \eta(t) \end{pmatrix} = \begin{pmatrix} v_h(t) \\ \eta_h(t) \end{pmatrix} + \begin{pmatrix} v_p \\ \eta_p \end{pmatrix} \varphi(t). \tag{2.6}$$

The augmented state $\boldsymbol{q}$, incorporating the actuation variable, is thus

$$\boldsymbol{q} = \begin{pmatrix} v_h(y,t) \\ \eta_h(y,t) \\ \varphi(t) \end{pmatrix}, \tag{2.7}$$

and augmented operator ($\boldsymbol{A}$) and operator ($\boldsymbol{B}$) (see § 3) can be written

$$\boldsymbol{A} = \begin{pmatrix} \mathscr{L}_{OSS} & \mathscr{L}_{OSS}\boldsymbol{q}_p \\ 0 & 0 \end{pmatrix}, \quad \boldsymbol{B} = \begin{pmatrix} -\mathbf{q}_p \\ 1 \end{pmatrix}, \tag{2.8}$$

with

$$\mathscr{L}_{OSS} = \begin{pmatrix} \mathscr{L}_{OS} & 0 \\ \mathscr{L}_C & \mathscr{L}_{SQ} \end{pmatrix}, \tag{2.9}$$

and where the particular solution $\boldsymbol{q}_p$ is chosen to satisfy the numerically convenient equation $\mathscr{L}_{OSS}\boldsymbol{q}_p = 0$ with a unity boundary condition on the wall-normal velocity at the wall. With this formulation the control signal becomes $u_c = \dot{\varphi}$.

2.2. *Stochastic disturbances*

2.2.1. *Modelling of the external disturbances*

The description of a dynamical system can also include a description of its input (external sources of excitations) and its output (measurements, possibly corrupted by noise). The performance of the state estimation relies on the construction of a proper model for the flow disturbances. If the external sources of perturbations in the flow are identified well, it becomes an easy task to estimate the flow evolution using a dynamic model of the system.

The external sources of perturbations in typical aeronautical applications can be wall roughness, acoustic waves, and free-stream turbulence. In the case where the sensors are distributed over a strip in the boundary layer, upstream instabilities can generate waves that are to be considered as disturbances to the estimator.

We will assume the external disturbance forcing $\boldsymbol{f} = (f_1, f_2, f_3)^T$ in (2.5) to be a zero-mean stationary white Gaussian process with auto-correlation

$$E[f_j(x, y, z, t) f_k(x + r_x, y', z + r_z, t') = \underbrace{\delta(t - t')}_{\text{Temporal}} \underbrace{Q_{f_j f_k}(y, y', r_x, r_z)}_{\text{Spatial}},$$

where $\delta(\cdot)$ denotes the Dirac δ-function.

The remaining property to be described is the spatial extent of the two-point one-time auto-correlation of $\boldsymbol{f}$ over the whole domain

$$Q_{f_j f_k}(y, y', r_x, r_z) = E[f_j(x, y, z, t) f_k(x + r_x, y', z + r_z, t)].$$

The corresponding quantity in Fourier space is a covariance operator, obtained for any wavenumber pair $\{k_x, k_z\}$ via the following integration over the homogeneous directions:

$$R_{f_j f_k}(y, y', k_x, k_z) = \int\int Q_{f_j f_k}(y, y', r_x, r_z) \mathrm{e}^{-\mathrm{i}(k_x r_x + k_z r_z)} \mathrm{d}r_x \, \mathrm{d}r_z.$$

Our model for the covariance of $\boldsymbol{f}$ assumes that the disturbance has a localized structure in space (i.e. the two-point correlation of the disturbance decays exponentially with distance) and that the correlations between forcing terms on different velocity components are zero. We assume a model for the covariance of the external forcing $\boldsymbol{f}$ of the form

$$R_{f_j f_k}(y, y', k_x, k_z) = d(k_x, k_z)\, \delta_{jk} \mathscr{M}^y(y, y'), \tag{2.10}$$

where

$$d(k_x, k_z) = \exp\left[-\left(\frac{k_x - k_x^0}{d_x} \right)^2 - \left(\frac{k_z - k_z^0}{d_z} \right)^2 \right]. \tag{2.11}$$

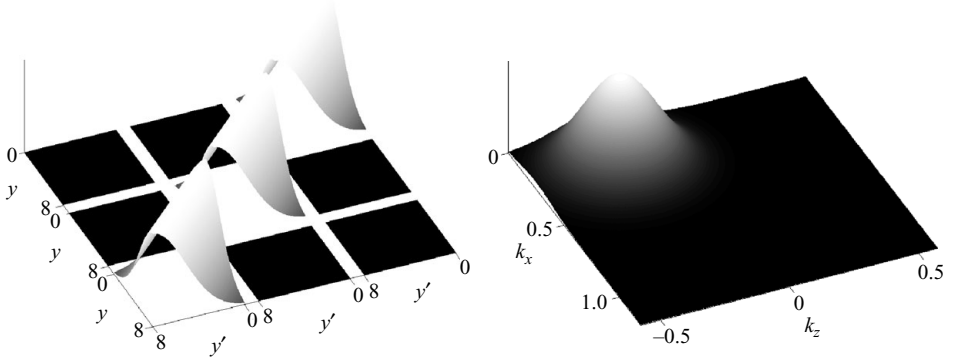

FIGURE 1. (*a*) The covariance of $\boldsymbol{f}$, for the FSC problem (cases 12–13 in table 1). From top to bottom and right to left each square represent the covariance for f_1, f_2, and f_3. (*b*) The wavenumber-space amplitude function. The peak is set at $\{0.25, -0.25\}$, about the mode that is triggered in the FSC simulations.

The model parameters k_x^0 and k_z^0 can be used to locate the peak energy of the disturbances in Fourier space, and d_x and d_z to tune the width of this peak. These parameters are specific for each flow case, e.g. for a typical Tollmien–Schlichting (TS)-wave the peak energy will be at $k_x^0 = 0.3$ and $k_z^0 = 0$, or for a typical streamwise streak, the choice will be $k_x^0 = 0$ and $k_z^0 = 0.49$.

The y-variation of $R_{f_j f_k}$ is given by the function

$$\mathscr{M}^y(y, y') = \exp\left[-\frac{(y - y')^2}{2d_y}\right], \tag{2.12}$$

where the design parameter d_y governs the width of the two-point correlation of the disturbance in the wall-normal direction. A common choice of the stochastic model has been to consider an uncorrelated model in the wall-normal direction. However, in Hœpffner *et al.* (2005) it was shown that better estimator performance could be achieved by using a physically motivated stochastic model similar to the model described in this section. The model-specific parameters for all flow cases presented are given in table 2 below.

Other forms for $d(k_x, k_z)$ are also possible, and may be experimented with in future work. Note that we will denote $\boldsymbol{R} = \boldsymbol{R}_{ff} = \mathrm{diag}(R_{f_1 f_1}, R_{f_2 f_2}, R_{f_3 f_3})$ in the sections that follow. The covariance of $\boldsymbol{f}$ is shown in figure 1.

2.2.2. *Sensors and sensor noise*

The measurements used in this study are the streamwise and spanwise shear stresses and the wall pressure fluctuations defined as

$$\tau_x = \tau_{xy}|_{\mathrm{wall}} = \frac{1}{Re}\left.\frac{\partial u}{\partial y}\right|_{\mathrm{wall}} = \frac{1}{Re}\frac{\mathrm{i}}{k^2}(k_x \mathrm{D}^2 v - k_z \mathrm{D}\eta)|_{\mathrm{wall}},$$

$$\tau_z = \tau_{zy}|_{\mathrm{wall}} = \frac{1}{Re}\left.\frac{\partial w}{\partial y}\right|_{\mathrm{wall}} = \frac{1}{Re}\frac{\mathrm{i}}{k^2}(k_z \mathrm{D}^2 v + k_x \mathrm{D}\eta)|_{\mathrm{wall}},$$

$$p = p|_{\mathrm{wall}} = \frac{1}{Re}\frac{1}{k^2}\mathrm{D}^3 v|_{\mathrm{wall}}.$$

which yields the following measurement matrix $\boldsymbol{C}$

$$\boldsymbol{C} = \frac{1}{Re}\frac{1}{k^2}\begin{pmatrix} \mathrm{i}k_x \mathrm{D}^2|_{\mathrm{wall}} & -\mathrm{i}k_z \mathrm{D}|_{\mathrm{wall}} \\ \mathrm{i}k_z \mathrm{D}^2|_{\mathrm{wall}} & \mathrm{i}k_x \mathrm{D}|_{\mathrm{wall}} \\ \mathrm{D}^3|_{\mathrm{wall}} & 0 \end{pmatrix}.$$

Hœpffner *et al.* (2005) discussed how the estimator performance degrades when different measurements are left out.

Each of the three measurements is assumed to be corrupted by random sensor noise processes, the amplitude of which is determined by the assumed quality of the sensors. The covariance of the sensor noise vector $\boldsymbol{g}$ can thus be described in Fourier space by a 3×3 matrix $\boldsymbol{G}$ where the diagonal elements α_ι^2 are the variances of the sensor noise assumed to be associated with each individual sensor. The covariance for each sensor can be written in the following form:

$$R_{g_\iota(t),g_\kappa(t')} = \delta_{\iota\kappa}\delta(t-t')\alpha_\iota^2, \tag{2.13}$$

where $\delta_{\iota\kappa}$ denotes the Kronecker delta. Thus, in the present work, we assume that the sensor noise is uncorrelated in both space and time.

When the signal-to-noise ratio is low, the measured signal must be fed back only gently into the estimator, lest the sensor noise disrupt the estimator. When the signal-to-noise ratio is high, the measured signal may be fed back more aggressively into the estimator, as the fidelity of the measurements can be better trusted. For a given covariance of the external disturbances, the tuning of the assumed overall magnitude of the sensor noise in the Kalman filter design thus provides a natural 'knob' to regulate the magnitude of the feedback into the estimator.

3. Compensation

The system is now described: its dynamics is governed by (2.2), it is excited by external sources of disturbance as in (2.11) and the sensor information is corrupted by noise as in (2.13). We can now apply the procedure of LQG control and estimation governed by system (2.5).

3.1. *Controller*

To construct an optimization problem we need to define an objective function. The performance measure for optimality is chosen as a weighted sum of the flow kinetic energy and the control effort. We thus aim to prevent small disturbances from growing, and achieve this goal with the minimum possible actuation energy. The objective functional is thus

$$J = \int_0^\infty \left(\boldsymbol{q}^* \boldsymbol{Q}\boldsymbol{q} + l^2 u_c^* u_c\right) \mathrm{d}t \tag{3.1}$$

where l^2 is included to penalize the time derivative of the control $u_c = \dot{\varphi}$, and

$$\boldsymbol{Q} = \begin{pmatrix} \boldsymbol{Q} & \boldsymbol{Q}\boldsymbol{q}_p \\ \boldsymbol{q}_p^* \boldsymbol{Q} & (1+r^2)\boldsymbol{q}_p^* \boldsymbol{Q}\boldsymbol{q}_p \end{pmatrix} \tag{3.2}$$

where the term r^2 is an extra penalty on the control signal itself. The operator $\boldsymbol{Q}$ represents the energy inner-product in (v, η) space

$$\begin{pmatrix} v^* & \eta^* \end{pmatrix} \boldsymbol{Q} \begin{pmatrix} v \\ \eta \end{pmatrix} = \frac{1}{8k^2}\int_0^\infty \left(k^2|v|^2 + \left|\frac{\partial v}{\partial y}\right|^2 + |\eta|^2\right) \mathrm{d}y, \tag{3.3}$$

with $k^2 = k_x^2 + k_z^2$.

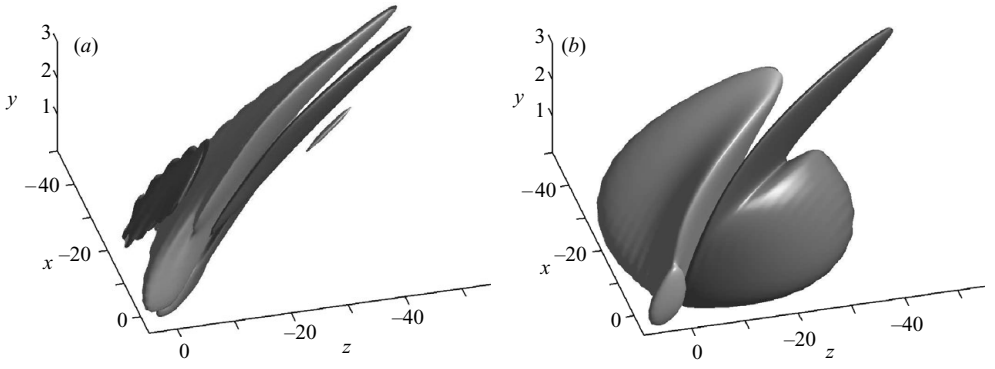

FIGURE 2. Steady-state control convolution kernels relating the flow state (*a*) $\hat{v}$ and (*b*) $\hat{\eta}$ to the control at $\{x=0,\ y=0,\ z=0\}$ on the wall. Positive (dark) and negative (light) isosurfaces with isovalues of $\pm 20\%$ of the maximum amplitude for each kernel are illustrated. The kernels correspond to cases 12–13 in tables 1 and 3.

We now want to find the optimal $\boldsymbol{K}$ that feeds back the state to update the control $u_c = \boldsymbol{K}\boldsymbol{q}$. It can be found as the solution of an algebraic Riccati equation (ARE)

$$\boldsymbol{A}^*\boldsymbol{X} + \boldsymbol{X}\boldsymbol{A} - \frac{1}{l^2}\boldsymbol{X}\boldsymbol{B}_2\boldsymbol{B}_2^*\boldsymbol{X} + \boldsymbol{Q} = 0 \tag{3.4}$$

where $\boldsymbol{X}$ is the unique non-negative self-adjoint solution. Note that the linear feedback law does not depend on the disturbances present in the flow and is thus computed once and for all for a given objective function and base flow. The optimal control gain $\boldsymbol{K}$ is

$$\boldsymbol{K} = -\frac{1}{l^2}\boldsymbol{B}_2^*\boldsymbol{X}. \tag{3.5}$$

A sufficient range of wavenumber pairs is computed and after Fourier transformation in both horizontal directions, we obtain physical-space control convolution kernels. Examples of such control kernels are depicted in figure 2.

3.2. *Estimator*

We build an estimator analogous to the dynamical system (2.5) as

$$\begin{aligned} \dot{\hat{\boldsymbol{q}}} &= \boldsymbol{A}\hat{\boldsymbol{q}} + \boldsymbol{B}_2 u_c - \boldsymbol{L}(\boldsymbol{y} - \hat{\boldsymbol{y}}), \quad \hat{\boldsymbol{q}}(0) = \hat{\boldsymbol{q}}_0, \\ \hat{\boldsymbol{y}} &= \boldsymbol{C}\hat{\boldsymbol{q}}, \end{aligned} \tag{3.6}$$

where $\hat{\boldsymbol{q}}$ is the estimated state and $\hat{\boldsymbol{y}}$ represents the measurements in the estimated flow.

Kalman filter theory, combined with the models outlined in § 2.2.1 and § 2.2.2 for the statistics of the unknown external forcing $\boldsymbol{f}$ and the unknown sensor noise $\boldsymbol{g}$ respectively, provides a convenient and mathematically–rigorous tool for computing the feedback operator $\boldsymbol{L}$ in the estimator described above such that $\hat{\boldsymbol{q}}(t)$ converges to an accurate approximation of $\boldsymbol{q}(t)$ (see e.g. Lewis & Syrmos 1995, pp. 463–470). Note that the volume forcing $\boldsymbol{v}_e = \boldsymbol{L}(\boldsymbol{y} - \hat{\boldsymbol{y}})$ used to apply corrections to the estimator trajectory is proportional to the measurement difference in the flow and in the estimator $\tilde{\boldsymbol{y}} = \boldsymbol{y} - \hat{\boldsymbol{y}}$.

The problem reduces to solving an algebraic Riccati equation similar to equation (3.4):

$$0 = \boldsymbol{A}\boldsymbol{P} + \boldsymbol{P}\boldsymbol{A}^* - \boldsymbol{P}\boldsymbol{C}^*\boldsymbol{G}^{-1}\boldsymbol{C}\boldsymbol{P} + \boldsymbol{B}_1\boldsymbol{R}\boldsymbol{B}_1^*, \tag{3.7}$$

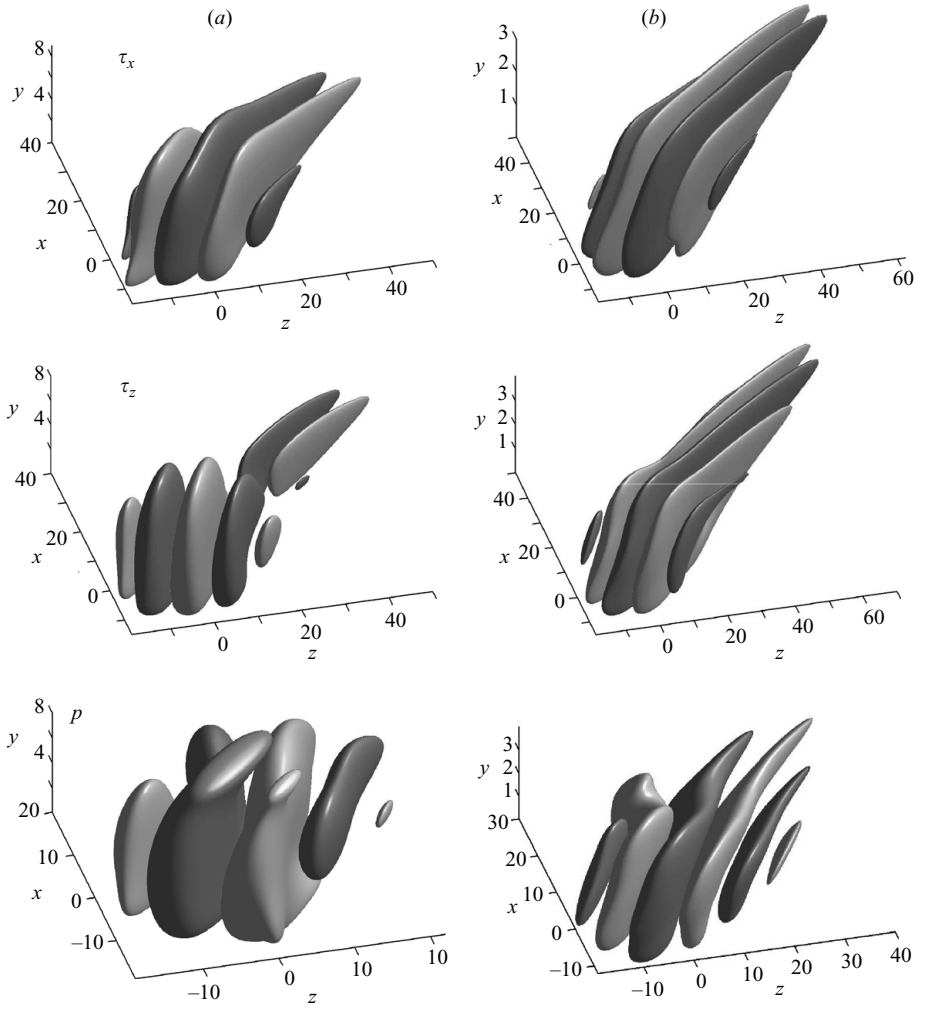

FIGURE 3. Steady-state estimation convolution kernels relating the measurements τ_x, τ_z, and p at the point $\{x=0,\ y=0,\ z=0\}$ on the wall to the estimator forcing in the interior of the domain for the evolution equation for the estimate of (*a*) $\hat{v}$ and (*b*) $\hat{\eta}$. Positive (dark) and negative (light) isosurfaces with isovalues of $\pm 10\%$ of the maximum amplitude for all kernels illustrated. The kernels correspond to case 13 in tables 1 and 3.

where $\boldsymbol{P}$ is the unique non-negative self-adjoint solution. The optimal gain $\boldsymbol{L}$ that minimizes the expected energy of the state estimation error at steady state is

$$\boldsymbol{L} = -\boldsymbol{P}\boldsymbol{C}^{*}\boldsymbol{G}^{-1}. \tag{3.8}$$

Estimation convolution kernels are exemplified in figure 3.

3.3. *Extension to spatially developing flows*

When solving the linear control problem and computing optimal control and estimation gains we have linearized about a base flow profile at a specific streamwise position, hence assuming a parallel base flow. However, owing to the non-parallel base flows in the DNS, errors will be introduced when the control signal and estimation forcing are computed. Based on findings in Högberg & Henningson (2002), Högberg

Case	Flow	Perturbation	Estimation	Control		
			$x_m \in$	r^2	l	$x_c \in$
0	A	Eigenmode				
1	A	Eigenmode		0	10^2	[0, 25.14]
2	A	Eigenmode	[0, 25.14]	0	10^2	[0, 25.14]
3	B	TS-wave				
4	B	TS-wave		0	10^2	[100, 250]
5	B	TS-wave	[0, 100]	0	10^2	[100, 250]
6	C	Optimal				
7	C	Optimal		0	10^2	[300, 450]
8	C	Optimal	[0, 300]	0	10^2	[300, 450]
9	C	Optimal		0	10^2	[300, 750]
10	C	Optimal	[0, 300]	0	10^2	[300, 750]
11	D	Random				
12	D	Random		0	10^2	[175, 325]
13	D	Random	[40, 150]	0	10^2	[175, 325]
14	E	Stationary				
15	E	Stationary		0	10^2	[150, 300]
16	E	Stationary	[40, 150]	0	10^2	[150, 300]

Letter	Flow	Resolution	Box	Fringe				
				x_{start}	x_{mix}	Δ_{mix}	Δ_{rise}	Δ_{fall}
A	Temporal FSC	$4 \times 129 \times 4$	$25.14 \times 20 \times 25.14$					
B	Spatial Blasius	$576 \times 65 \times 4$	$1128 \times 20 \times 12.83$	928	928	50	30	15
C	Spatial Blasius	$576 \times 65 \times 4$	$1128 \times 20 \times 12.83$	1028	1028	40	100	20
D	Spatial FSC	$192 \times 49 \times 48$	$500 \times 8 \times 251.4$	350	400	40	100	20
E	Spatial FSC	$768 \times 65 \times 24$	$500 \times 8 \times 25.14$	350	400	40	100	20

TABLE 1. Detailed information about the simulations performed in this study. Both the control and estimation kernels are computed based on a velocity profile from the centre of each domain except for cases 9–10 where the same control kernels were used as for cases 7–8. The rise and fall distance of the control region and the measurement region are always $\Delta x = 5$. The domain x_m denotes the measurement region used in the estimator and the domain x_c denotes the region where blowing and suction is applied in the control part of the simulations. The estimator model parameters for the different cases are given in table 3.

et al. (2003*b*, *c*) , and Chevalier *et al.* (2006) it was expected that the controller and the estimator had some robustness properties with respect to changes in the base flow profile. The fact that the convolution kernels themselves, for proper choices of parameters, are localized indicates that only local information is needed, which relaxes the requirement of constant base flow profile. For almost all control and estimation gains, the base flow profile in the centre of the control and measurement regions has been used. For the longer control interval in the optimal perturbation flow case, the same gains were used as for the shorter interval.

The control and estimation convolution kernels for the Falkner–Skan–Cooke boundary layer flow, corresponding to cases 12–13 in table 1, are depicted in figures 2 and 3. Both the control and estimation kernels were computed with a physical box size of $100 \times 10 \times 125.7$ with $192 \times 65 \times 125.7$ Fourier, Chebyshev, Fourier modes. Furthermore, the kernels were based on the mean flow at $x = 95$ and $x = 200$ for the estimation and control respectively. For all cases studied the general behaviour of the control kernels is the same in the sense that they all reach upstream in order to

obtain information about the perturbations present in the flow. Correspondingly the estimation kernels reach downstream from the point of sensing yielding information on how each measurement should force the estimator. However, owing to the differing base flows and their inherent instabilities the kernels will differ in shape and extent. The streamwise length of the sensing/actuation strip is limited above because of the non-parallel base flow, and below by the physical extent of the convolution kernels. The control and estimation region lengths used in this paper for the spatial flow cases were chosen in this range. Note that the performance of the controller/estimator degrades with parameters outside this limit but will generally still produce reasonable results.

4. Numerical issues

4.1. *Direct numerical simulations*

All direct numerical simulations have been performed with the code reported in Lundbladh, Henningson & Johansson (1992) and Lundbladh *et al.* (1999), which solves the incompressible Navier–Stokes equations

$$\left.\begin{aligned} \frac{\partial \boldsymbol{u}}{\partial t} &= NS(\boldsymbol{u}) + \lambda(x)(\boldsymbol{u} - \boldsymbol{u}_\lambda) + \boldsymbol{F}, \\ \nabla \cdot \boldsymbol{u} &= 0, \end{aligned}\right\} \tag{4.1}$$

by a pseudo-spectral approach. The velocity vector $\boldsymbol{u}$ is defined as $\boldsymbol{u} = (u, v, w)^T$. In the following we will divide the velocity field into a base flow $\boldsymbol{U} = (U, V, W)$ and a disturbance part $\boldsymbol{u}' = (u', v', w')$ so that $\boldsymbol{u} = \boldsymbol{U} + \boldsymbol{u}'$. In order to allow spatially developing flows, a fringe region technique as described in e.g. Nordström, Nordin & Henningson (1999) has been applied. This forcing is implemented in the term $\lambda(x)(\boldsymbol{u} - \boldsymbol{u}_\lambda)$, where $\lambda(x)$ is a non-negative function which is non-zero only in the fringe region located at the downstream end of the computational box. The outflow and inflow conditions are determined by the desired velocity distribution $\boldsymbol{u}_\lambda$. The other forcing term $\boldsymbol{F} = [F_1, F_2, F_3]^T$ is used e.g. to enforce a parallel base flow in temporal simulations, or to introduce perturbations in the spatial simulations.

At the lower wall a no-slip boundary condition is applied, where it is also possible to apply zero-mass-flux blowing and suction. An asymptotic free-stream boundary condition is used to limit the computational box in the wall-normal direction, at a constant height from the lower wall (see e.g. Malik, Zang & Hussaini 1985).

The computational domain is discretized in space by Fourier series in both horizontal directions and with Chebyshev polynomials in the wall-normal direction. The time integration uses a four-step low-storage third-order Runge–Kutta method for the advective and forcing terms whereas the viscous terms are treated by a Crank–Nicolson method. The incompressibility condition is enforced implicitly by expressing the flow state in the wall-normal-velocity and wall-normal-vorticity state space.

4.2. *Temporal simulations*

When needed, we add a volume forcing vector $\boldsymbol{F} = [F_1, F_2, F_3]^T$ to enforce a parallel base flow, defined as

$$\left.\begin{aligned} F_1 &= -\frac{\partial U(y,t)}{\partial t} - \frac{1}{Re}\frac{\partial^2 U(y,t)}{\partial y^2}, \\ F_2 &= 0, \\ F_3 &= -\frac{1}{Re}\frac{\partial^2 W(y,t)}{\partial y^2}. \end{aligned}\right\} \tag{4.2}$$

The velocity profiles $U(y,t)$ and $W(y,t)$ are given for a spatial position x_r. To also allow for a moving frame we make the variable transformation $x_r = x_0 + ct$ where c is the reference frame speed, and let $U(x_r, y) = U(x_0 + ct, y) = U(t, y)$.

4.3. *Spatial simulations*

4.3.1. *Fringe region*

By adding the fringe forcing mentioned in §4.1 we can enforce flow periodicity and thus apply spectral methods, allowing us to solve spatially developing flows. The fringe function is defined as

$$\lambda(x) = \lambda_{\max}\left[S\left(\frac{x - x_{\text{start}}}{\Delta_{\text{rise}}}\right) - S\left(\frac{x - x_{\text{end}}}{\Delta_{\text{fall}}} + 1\right)\right] \tag{4.3}$$

where the ramping function S is defined as

$$S(x) = \begin{cases} 0, & x \leqslant 0, \\ 1/\left[1 + \exp\left(\dfrac{1}{x-1} + \dfrac{1}{x}\right)\right], & 0 < x < 1, \\ 1, & x \geqslant 0. \end{cases} \tag{4.4}$$

The parameters x_{start} and x_{end} define the start and end locations of the fringe domain, whereas the parameters Δ_{rise} and Δ_{fall} define the rise and fall distance of the fringe function.

In order to enforce the inflow boundary condition at the downstream end of the domain we construct the following blending function which gives a smooth interpolation between two velocity profiles. Let the velocity components be defined as

$$\left.\begin{aligned} u_\lambda &= U(x,y) + [U(x - l_x, y) - U(x,y)]\, S\left(\frac{x - x_{\text{mix}}}{\Delta_{\text{mix}}}\right) + u'_f(x - l_x, y, z, t), \\ w_\lambda &= W(x,y) + [W(x - l_x, y) - W(x,y)]\, S\left(\frac{x - x_{\text{mix}}}{\Delta_{\text{mix}}}\right) + w'_f(x - l_x, y, z, t), \end{aligned}\right\} \tag{4.5}$$

where l_x is the box length in the streamwise direction. The parameters x_{mix} and Δ_{mix} are both blending parameters. The former is the start of the blending region and the latter is the rise distance of the blending. Additional forcing to add streaks or different wave forms can be added through the velocity components (u'_f, v'_f, w'_f) directly in the fringe.

4.3.2. *Perturbations*

To introduce perturbations into the spatially evolving flow an external volume force can be applied locally in the computational domain. This forcing can either be applied in the fringe region, as for the optimal disturbance and the TS-wave case, or in the physical flow domain.

In order to introduce unsteady perturbations in the physical computational domain, we use a random forcing, acting only on the wall-normal component of the momentum equations:

$$F_2^{\text{rand}} = a_t \exp[-((x - x_{\text{center}})/x_{\text{scale}})^2 - (y/y_{\text{scale}})^2]\, f(z,t), \tag{4.6}$$

where

$$f(z,t) = [(1 - b(t))h^k(z) + b(t)h^{k+1}(z)] \tag{4.7}$$

Parameter	Cases 3–5	Cases 6–10	Parameter	Cases 11–13	Cases 14–16
x_f	−201.06	−158.16	x_0	20.95	20.95
ω	0.06875	0	a_t	0.001	
k_z	0	0.4897	a_s		0.0036
a_s	10^{-5}		x_{scale}	10	10
t_s	0	y_{scale}	1	1	
t_r	20		z_{scale}		−25.14
			z_{center}	0	0
			l_{skew}		1
			n_{modes}	21	
			t_{dt}	1	

TABLE 2. Volume forcing parameters for the spatial simulations. Note that negative coordinates indicate positions upstream of the inflow boundary.

and

$$k = \text{floor}(t/t_{\text{dt}}), \quad b(t) = 3p^2 - 2p^3, \quad p = t/t_{\text{dt}} - k, \tag{4.8}$$

where floor denotes rounding to the next smaller integer, and $h^k(z)$ is a Fourier series of unit-amplitude functions with random phase generated at every time interval k. Within each time interval t_{dt}, the function $b(t)$ ramps the forcing smoothly in time. The maximum amplitude is determined by a_t and the forcing is exponentially decaying in both the streamwise and wall-normal directions centred at x_{centre}. The number of modes with non-zero amplitude is determined by the parameter n_{modes}. This forcing has been used to generate the travelling crossflow vortices described as cases 11–13 in table 1 with the corresponding parameters given in table 2.

Disturbances are generated in the fringe region through prescribing the components (u'_f, v'_f, w'_f) in equation (4.5). Since we are looking at the evolution of linear disturbances, these components can be taken as the eigenfunctions of the parabolized stability equations, known as the PSE (Bertolotti, Herbert & Spalart 1992; Herbert 1997). Input to the eigenvalue problem is a given real frequency ω, an appropriate Reynolds number Re and a real spanwise wavenumber k_z^f. A set of equations valid for both algebraically and exponentially growing disturbances was derived in Levin (2003), capturing the different scales associated with the two growth scenarios. Having obtained the complex eigenvalues $k_x^f(x)$ and the eigenfunctions $\hat{\boldsymbol{q}} = (\hat{u}(x, y), \hat{v}(x, y), \hat{w}(x, y))^T$ from the solution of the PSE, one can readily formulate the forcing applied in the fringe as the real part of

$$q'_f = a_s \hat{q}(x, y) \exp\left(\mathrm{i}Re \int_{x_f}^{x} k_x^f(\xi)\,\mathrm{d}\xi + \mathrm{i}k_z^f z - \mathrm{i}\omega t\right) S\left(\frac{t - t_s}{t_r}\right) \tag{4.9}$$

where x_f is typically the start of the fringe region and a_s is the amplitude of the disturbance. The ramping function S is given by equation (4.4) and t_s and t_r are used as time ramping parameters.

4.3.3. *Zero-mass-flux actuation*

As the numerical model in the DNS does not allow net inflow or outflow, we have to enforce a zero mass flux through the actuation strip by the transformation

$$\hat{\varphi}(x, z) = (\varphi(x, z) + c)H(x), \tag{4.10}$$

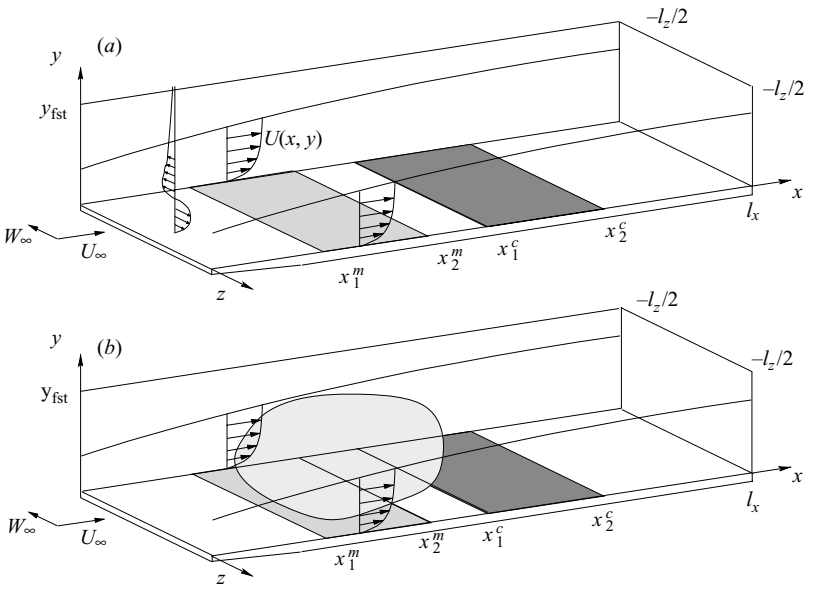

FIGURE 4. Compensator configuration. (*a*) The 'real' flow where the light grey rectangle along the wall is the measurement region ($x \in [x_1^m, x_2^m]$) and the corresponding dark grey rectangle is the control area ($x \in [x_1^c, x_2^c]$). At the beginning of the box a perturbation is indicated as a function of the wall-normal direction. This perturbation will evolve as we integrate the system in time. (*b*) The estimated flow system. Here the volume force that is based on the wall measurements and the estimation gains is shown as a grey cloud in the computational domain.

where

$$c = -\frac{\int_z \int_x \varphi(x, z) H(x) \, \mathrm{d}x \, \mathrm{d}z}{l_z \int_x H(x) \, \mathrm{d}x} \tag{4.11}$$

and

$$H(x) = S\left(\frac{x - \left(x_c - l_x^c/2\right)}{\Delta x}\right) - S\left(\frac{x - \left(x_c + l_x^c/2\right)}{\Delta x}\right). \tag{4.12}$$

The parameter $S(x)$ is defined as in equation (4.4) and x_c denotes the centre of the control interval. Parameters l_x^c and l_z^c are respectively the length and width of the control domain and Δx is the rise and fall distance of the actuation.

4.4. *Compensator algorithm*

The compensator algorithm is depicted in figure 4. The 'real' flow could be an experimental setup where only wall information is extracted. In our studies the 'real' flow is represented by a DNS. The estimator is another DNS, which is used to recover the state from sensor information. The compensation algorithm can be sketched in the following steps:

(*a*) take wall measurements in both real and estimated flows

(*b*) compute the estimator volume forcing based on precomputed estimation gains and the difference of the wall measurements from the real and estimated flows

(*c*) apply the volume forcing to the estimator flow to make it converge to the real flow

Parameter	Cases				
	3	5	8 & 10	13	16
k_x^0	0.25	0.28	0.0	0.25	0.25
k_z^0	−0.25	0.0	0.49	−0.25	−0.25
d_x	0.10	0.25	0.15	0.20	0.20
d_y	0.50	0.10	0.50	0.50	0.50
d_z	0.10	0.25	0.15	0.20	0.20
α_{τ_x}	29.56	4.0	0.20	0.20	0.20
α_{τ_z}	2.21	0.30	0.20	0.20	0.20
α_p	14783	2000	300	30000	30000

TABLE 3. Estimator model parameters. The parameters k_x^0, k_z^0, d_x, d_y, and d_z all relate to the covariance model of the external disturbances and the parameters α_{τ_x}, α_{τ_z}, and α_p relate to the modelling of the sensor noise. See § 2.2 for definitions of the parameters.

(*d*) compute the control signal as a feedback of the reconstructed state in the estimator

(*e*) apply the control signal in both the real and estimated flows.

5. Flow cases

In order to evaluate the compensator performance in transitional flows we test a range of different flow cases. To ease the comparison with the full information controller results reported in Högberg & Henningson (2002) we study some of the same flow cases and the same control parameter $l^2 = 100$ has been used. However, some control regions have been moved further downstream to fit a measurement region also into the computational domain. Note that in principle we could have overlapping control and measurement regions. The computational parameters for each flow type are listed in tables 1, 2 and 3.

5.1. *Single eigenmode*

To validate the numerical implementation of the control and the estimator forcing we studied a temporal FSC boundary layer flow where the Reynolds number at the beginning of the simulation box was $Re = 337.9$ with a free-stream crossflow velocity component $W_\infty = 1.44232\, U_\infty(x = 0)$ and a favourable pressure gradient $m = 0.34207$ as defined in § 2.1. The same flow setup is also studied in a spatial setting in § 5.4. In the case of temporal flow the measurement and control regions overlap since they both extend over the complete wall.

The initial disturbance is the unstable eigenfunction associated with the eigenvalue $c = -0.15246 + \mathrm{i}0.0382$ that appears at $k_x = 0.25$ and $k_z = -0.25$. The exponential energy growth of the uncontrolled eigenmode is depicted in figure 5 as a thick solid line. In the same figure the full information controller is plotted as a thick dashed line and the disturbance energy decays rapidly in time and levels out. All thin lines are related to the compensator simulation. The thin solid line represents the disturbance energy in the estimator and it increases initially to quickly align with the energy growth of the actual state. This can also be viewed through the estimation error plotted as a thin dash-dotted line which decays exponentially in time. The compensator control is shown as the thin dashed line. Initially, when the estimated state is poor, the controller is not very efficient. However as the estimated state improves the compensator control also improves.

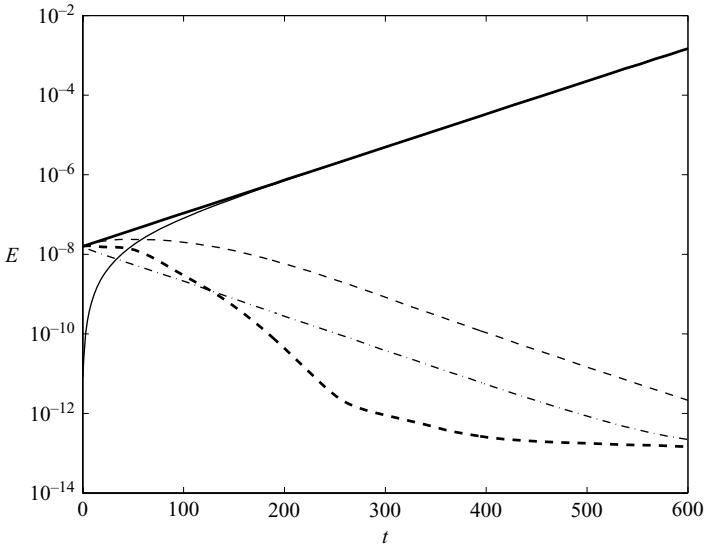

FIGURE 5. Time evolution of the perturbation energy of the uncontrolled unstable eigenmode at $k_x = 0.25, k_z = -0.25$ in an FSC boundary layer and the corresponding controlled system. Thick solid: uncontrolled energy growth (case 0). Thick dashed: full information control applied (case 1). Thin solid: energy growth in the estimator when no control is applied. Thin dash-dotted: the estimation error when no control is applied. Thin dashed: compensator control is applied (case 2). The simulations correspond to cases 0–2 in table 1.

5.2. *TS-wave*

The TS-wave perturbation is applied to a spatially developing Blasius boundary layer with an inflow Reynolds number of $Re = 1150$. This base flow can be obtained as a similarity solution described in § 2.1 with $m = 0$. The perturbations are introduced by means of forcing in the fringe region as described in § 4.3.2. Since the TS-wave is a pure two-dimensional instability, the spanwise wavenumber in (4.9) is $k_z^f = 0$. These waves are forced at the dimensionless oscillating frequency $F = 59$, related to the physical frequency ω by $F = 10^6 2\pi\omega\nu/U_\infty^2$. This value is chosen according to Levin (2003) where it was found to be the most unstable. The unstable area for this wave extends from Branch I at $x = -124$ ($Re \approx 949$) to branch II at $x = 621$ ($Re \approx 1854$). The measurement region is $x \in [0, 100]$ and the control region is $x \in [100, 250]$ so that they are both located in the exponential growth region. The simulation parameters correspond to cases 3–5 in table 1 and the parameters defining the fringe forcing are given in table 2.

Figure 6 shows the uncontrolled energy growth and decay as the solid thick line. Full information control, displayed as the thick dash-dotted line, performs perfectly, lowering the amplitude of the energy by approximately five decades. The estimator builds up energy levels throughout the whole estimation region, almost reaching the amplitude of the original flow. This is visualized as the thin solid line.

Note that the difference between the compensator control and full information control in figure 6 is exaggerated due to the logarithmic scale. In fact this difference is of the same order of magnitude as the energy difference between the real and estimated flow. By extending the estimation region (and moving the control region further downstream) one can achieve a closer agreement between the compensator and the full information controller. Note however that there is interest in controlling

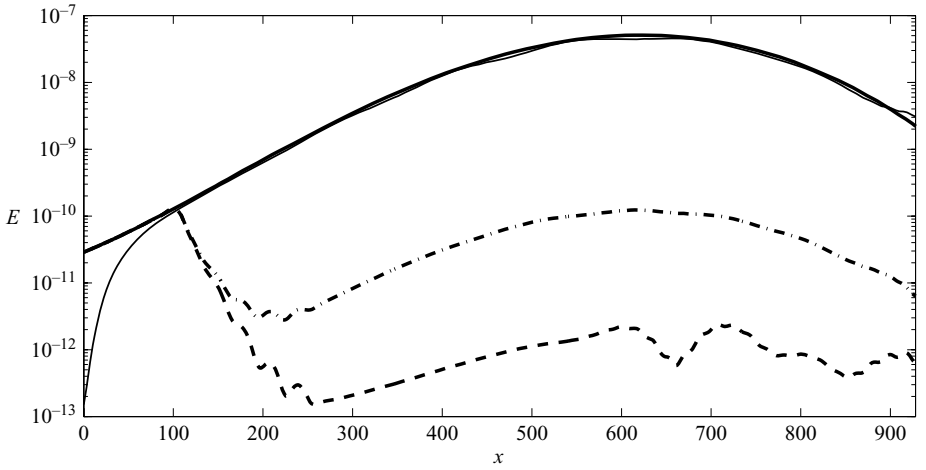

FIGURE 6. Spatial evolution of the perturbation energy of a TS-wave in a spatially growing boundary layer. Thick solid: uncontrolled energy growth. Thin solid: estimated flow energy. Dashed: full information control applied. Dash-dotted: compensator control applied.

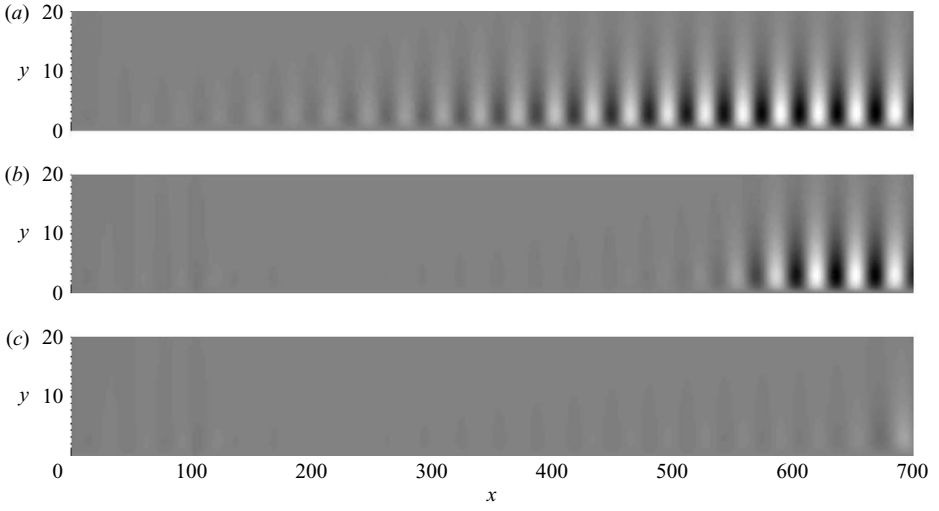

FIGURE 7. Snapshots of the wall-normal perturbation velocity for controlled and uncontrolled TS-waves. (*a*) The TS-wave with no control. (*b*) Compensator control applied during 15 TS-wave periods which corresponds to 926 time units. (*c*) Compensator control applied during 45 TS-wave periods. The unsteady wall blowing and suction effectively eliminates disturbances, with the result that the original TS-wave disturbances are advected out of the domain. The black to white scales lie within the interval $v \in [-9.87 \times 10^{-5}, 8.18 \times 10^{-5}]$.

the TS-wave evolution as far upstream as possible. Choosing the moderate estimation region length of 100, the compensator still lowers the energy levels by almost three decades.

Figure 7(*a*) shows a snapshot of an x–y-plane of the wall-normal uncontrolled velocity field. The forcing has been turned on long enough to let the waves propagate throughout the whole computational box. In figure 7(*b*) the compensator control has been active for 926 time units, corresponding to approximately fifteen periods of the

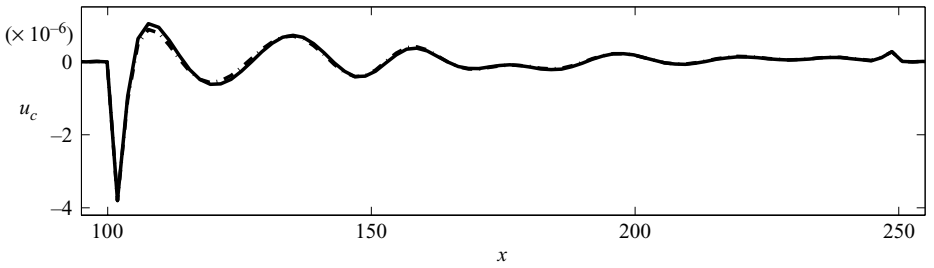

FIGURE 8. Control signal when the control has been turned on for 926 time units. Solid: full information control. Dash-dotted: compensator control.

forcing. At this instance of time there are still large-amplitude disturbances present far downstream, but as can be seen from figure 7(*c*), 30 periods later the contour levels of the disturbances are small throughout the whole domain. It is evident that the unsteady blowing and suction has effectively diminished the disturbances, leaving the remaining TS-wave to be advected out of the domain by the base flow.

Instantaneous control signals for the full information control and the compensator control are shown in figure 8. The control signals mimic waves with decaying amplitude in the streamwise direction. The large amplitude at the beginning of the control interval is due to the fact that the controller is effective within only a few wavelengths of the TS-wave, hence leaving large-amplitude control further downstream unnecessary.

5.3. *Optimal perturbation*

The compensator performance is also studied for transiently growing perturbations, also known as optimal perturbations after Butler & Farrell (1992). The spatial optimal perturbations in a Blasius boundary layer have been computed by Andersson, Berggren & Henningson (1999) and Luchini (2000). The optimal perturbation is introduced at $x = -158.16$ and then marched forward to $x = 0$ with the technique developed in Andersson *et al.* (1999). The perturbation is introduced in the fringe region to give the proper inflow condition, as described in § 4.3 and with the choice of parameters displayed in table 2. The perturbation is optimized to peak at $x = 237.24$.

The base flow is essentially the same as the one described in § 5.2, with the same box size but with a smaller fringe region and a lower Reynolds number. Here the local Reynolds number at the inflow is $Re = 468.34$ (Andersson *et al.* 2000). The simulation parameters are given in table 1 as cases 6–10.

Figure 9 shows the energy of the uncontrolled flow, estimated flow, full information control and compensator control once steady state has been reached. The compensator control reduces the disturbance energy to almost the same level as the full information control does. Here the energy is defined as

$$E = \int_0^{2\pi/k_z^0} \int_0^{\infty} (u^2 + v^2 + w^2)\,\mathrm{d}y\,\mathrm{d}z, \tag{5.1}$$

where the spanwise wavenumber is $k_z^0 = 0.4897$. Two different lengths of control regions have been implemented. Both types of controllers for both control intervals work well in reducing the perturbation energy. In the case with a narrow control strip the perturbation energy starts to grow again since a stronger component of the growing disturbance remains.

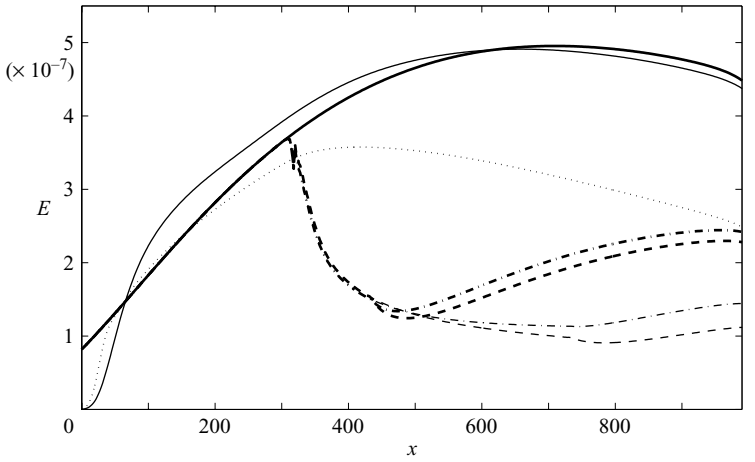

FIGURE 9. Spatial energy evolution of the optimal perturbation. Solid: no control. Thin solid: estimated flow energy employing stochastic forcing according to parameters given in table 3 but with $d_y = 2.0$. Thin dotted: estimated flow energy with spatially uncorrelated stochastic forcing. Thick dashed: full information control applied in region $x \in [300, 450]$. Thick dash-dotted: compensator control with measurement region $x \in [0, 300]$ and the control region $x \in [300, 450]$. Thin dashed: full information control applied in region $x \in [300, 725]$. Thin dash-dotted: compensator control with the measurement region $x \in [0, 300]$ and the control region $x \in [300, 725]$. The flow cases correspond to cases 6–10 in table 1.

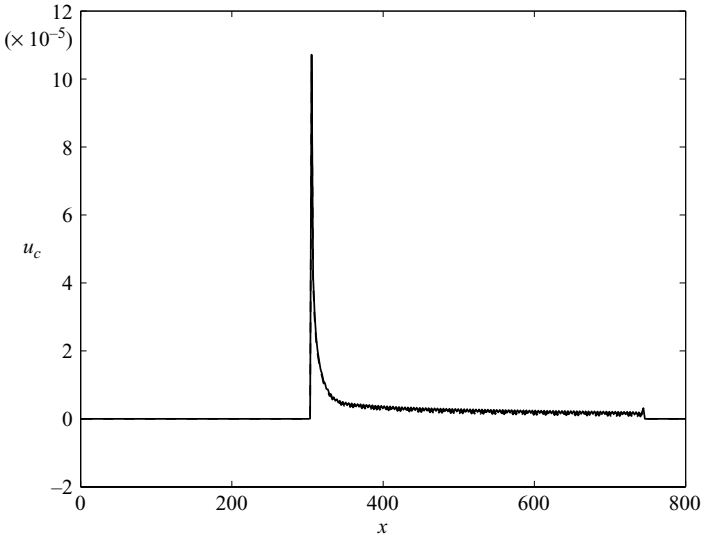

FIGURE 10. The control signal for the optimal disturbance case after the initial transient. Solid: full information control. Dashed: compensator control in domain. The simulations correspond to case 9 and 10 in table 1.

The control signals for the full information and compensator control cases, applied in the interval $x \in [300, 750]$, are depicted in figure 10. The actuation presents a peak at the beginning of the control region and then a fast decay which levels out progressively. A similar feature is reported in Cathalifaud & Luchini (2000) where control is applied over the whole domain.

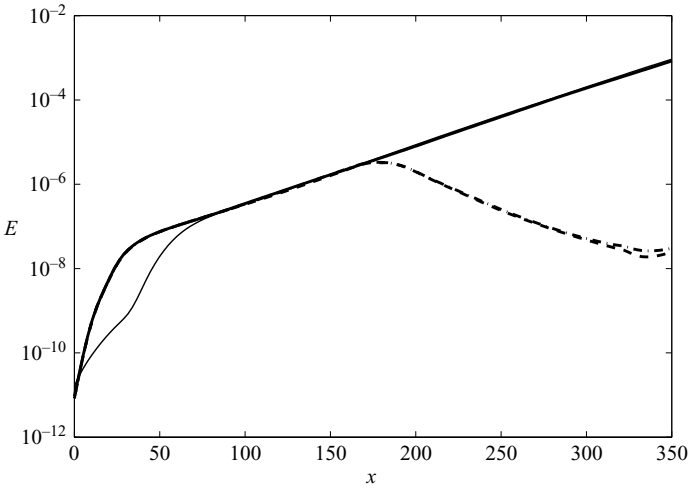

FIGURE 11. Time-averaged perturbation energy for crossflow vortices in a Falkner–Skan–Cooke boundary layer. Thick solid: uncontrolled. Dashed: full information control. Dash-dotted: compensator control. Thin solid: estimator energy. The simulations correspond to cases 11–13 in table 1.

5.4. *Travelling crossflow vortices*

The FSC boundary layer flow studied in this paper has been the subject of several other studies, for example Högberg & Henningson (1998) and Högberg & Henningson (2002). Originally it was an attempt to reproduce experimental results where travelling crossflow modes had been observed (see e.g. Müller & Bippes 1988). A random perturbation in space and time that generates crossflow vortices downstream is applied, as described in § 4.3.2. The specific numerical details can be found under cases 11–13 in tables 1 and 2.

In case 11 we compute the time evolution of the forcing as it develops downstream and forms the crossflow vortices. When the simulations have reached a statistically steady state the disturbance energy is sampled and averaged in time and the spanwise direction as shown in figure 11. The energy growth of the perturbation is shown as a black solid line. In case 12 we apply full information control. Exponential decay then replaces the uncontrolled exponential growth, as shown by the dashed line in figure 11. However almost adjacent to the downstream end of the control region the disturbances start to grow exponentially; this wave is unstable over the whole box, and resumes growth behind the control strip. In the same figure the perturbation energy for the compensator is plotted as a dash-dotted line.

In figure 12 the evolution in time of the perturbation energy, integrated throughout the computational box in space, is shown. The energy in the estimator is shown as a thin solid line which is zero at time $t = 0$ but as time evolves reaches the same level as the perturbation energy in the real flow. From figure 12 it is also evident that the estimator is able to adapt to the time variations of the perturbation energy.

The control gains are computed for the base flow at position $x = 250$, which is the centre of the control domain $x \in [175, 325]$. The estimator gains are centred at $x = 95$ and the measurements are taken in $x \in [40, 150]$. In figure 13(a) the uncontrolled flow for the wall-normal perturbation velocity is plotted at $y = 1.0$. The corresponding plot for the compensated flow is depicted in figure 13(b).

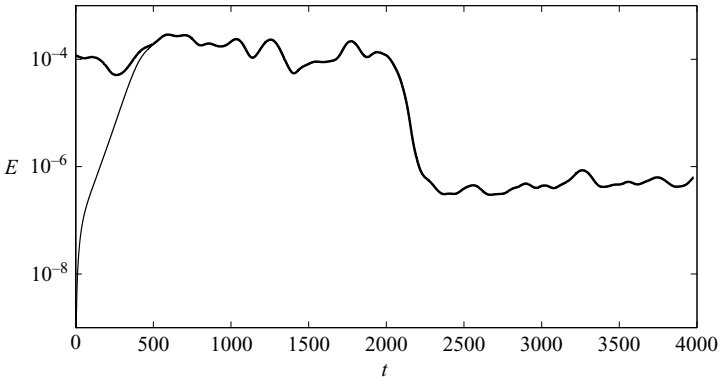

FIGURE 12. Time evolution of the disturbance energy integrated throughout the computational box. During the first 2000 time units the flow is uncontrolled. At time $t = 2000$ the compensator is turned on. Thick solid: energy in the flow. Thin solid: energy in the estimator.

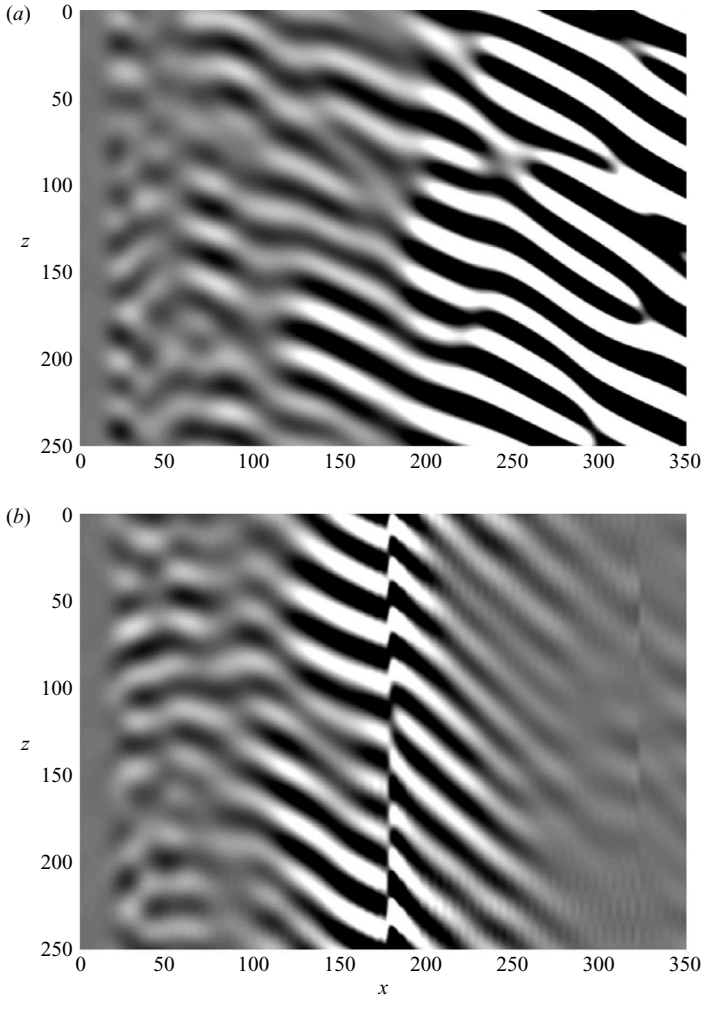

FIGURE 13. Snapshots of the wall-normal velocity component at $y = 1.0$. (*a*) The flow state. (*b*) The effect of the compensator control. In the controlled flow the actuation was applied in 2000 time units. The black to white scales lie within the interval $v \in [-0.00045, 0.00055]$.

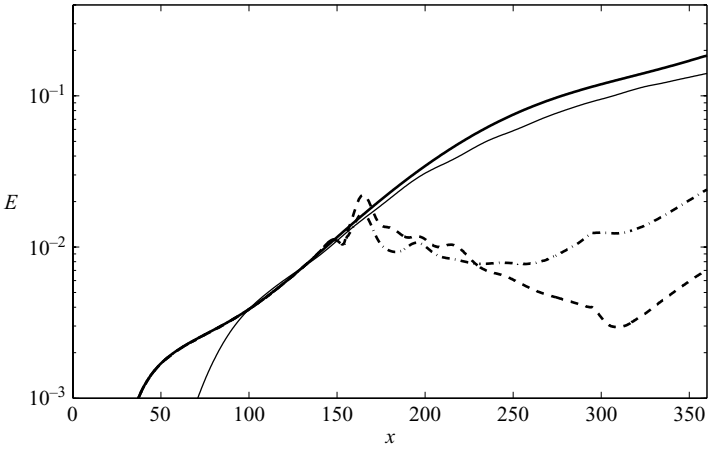

FIGURE 14. Perturbation energy growth for crossflow vortices in a Falkner–Skan–Cooke boundary layer. Thick solid: uncontrolled. Dashed: full information control. Dash-dotted: compensator control. Thin solid: estimator energy. The simulations correspond to cases 14–16 in table 1.

5.5. *Stationary crossflow vortices*

Stationary perturbations introduced at the beginning of the computational domain, with large enough amplitudes, will generate stationary nonlinearly saturated crossflow vortices that develop downstream.

The control acts in the interval $x \in [150, 300]$ and the control kernels are computed based on the mean flow at $x = 225$ with $l = 10^2$. The measurement region is in the interval $x \in [40, 150]$ and the estimation kernels are computed based on the base flow centred in that interval. The complete set of parameters for these simulations is given as cases 14–16 in table 1.

The full information control has been applied to both a flow with fully developed crossflow vortices throughout the computational domain and a flow where the control is turned on at the same time as the perturbation is first introduced in the upstream region. Both approaches give the same result after the initial transients, due to the control. However the transition phase in the former case requires smaller time steps due to stronger transients. There could also be a problem in the former case if too strong wall-normal velocities are generated, owing to technical limitations in the spectral code that is being used.

For estimation-based control, two approaches regarding the initial state of the estimator have been attempted. First the control is applied after a well-converged estimated state is obtained. This leads to full actuation strength immediately. To avoid a strong initial actuation, we turn on the estimator and control at the same time. The results shown here have been produced with the latter method.

The simulation is run until a stationary state has been reached and the corresponding energy is shown in figure 14. The thick solid line shows the perturbation energy and the thin line shows the corresponding estimator state energy. The dashed and dash-dotted lines show the full information and compensated control cases respectively. In both cases, oscillations in the upstream part of the control region indicate that there are nonlinear interactions taking place. As reported in Högberg & Henningson (2002), the full information control turns exponential growth into exponential decay, and downstream of the control region, new crossflow vortices

d_y	d_x	d_z	k_x^0	k_z^0	α_{τ_x}	α_{τ_z}	α_p	J_{τ_x}	J_{τ_z}	J_p
0.10	0.15	0.15	0.0	0.49	0.20	0.20	300	18.3619	21.5604	0.0562

TABLE 4. Reference values, according to integral (5.2), of the estimation gains for the streak instability. All gains in the comparison study are scaled to match these values for J_{τ_x}, J_{τ_z} and J_p respectively.

appear due to the inflectional instability. The compensator control never reaches exponential decay but, rather, maintains a more or less constant perturbation energy throughout the control interval.

5.6. *Impact of stochastic modelling on estimation*

We have seen that the performance of the estimator can be improved if the external excitation sources are described well by the stochastic model of § 2.2. The parameters given in table 3 are chosen to fit fairly well each specific perturbation for the different flow cases we have considered. In this section we perform a quantitative comparison of the estimator performance applied to the streaky flow case of § 5.3 for three sets of model parameters: the uncorrelated model, and the correlated model with two different correlation lengths in the wall-normal direction.

A first comparison of the estimation performance for different models was shown in figure 9. Using the correlated model with $d_y = 2.0$, the upstream part of the streak energy was overpredicted while the downstream part was slightly underpredicted, but yielding the lowest overall energy of the estimation error when compared to other choices of wall-normal correlation length parameter d_y. On the other hand the estimator built from the uncorrelated stochastic model has correct energy levels in the first half of the measurement region, but is simply not able to converge to a good estimate of the flow downstream, where the flow response has largest energy. Note that $d_y = 0.5$ gives the best compensator performance owing to its slightly better energy level match in the upstream region of the flow.

When changing the stochastic properties of the external forcing the strength of the resulting gains changes. In order to keep the strength of the gains at the same level, keeping in mind that they act directly as forcing terms in the estimator, we scale them to maintain a reference value of the integrated quantities:

$$J_\chi = \int_0^{L_z} \int_0^{L_x} \int_0^{y_\infty} L_\chi^2 \, \mathrm{d}y \, \mathrm{d}x \, \mathrm{d}z, \tag{5.2}$$

where χ represents the different measurements τ_x, τ_z and p. The integrated quantities of (5.2) for the reference stochastic model are given in table 4.

In figure 15 the time history of the difference in energy of the estimation error between the three stochastic models is shown. The solid and the dashed lines show the estimator results based on correlated stochastic forcing with the parameters $d_y = 2.0$ and $d_y = 0.5$ respectively, see equation (2.12). The dash-dotted line represents the uncorrelated stochastic forcing. All three estimators converge to reasonable energy levels, but the best performance is obtained with the parameter $d_y = 2.0$. For larger values of d_y the estimation error starts to increase again. Similar behaviour is observed for the other flow perturbation scenarios.

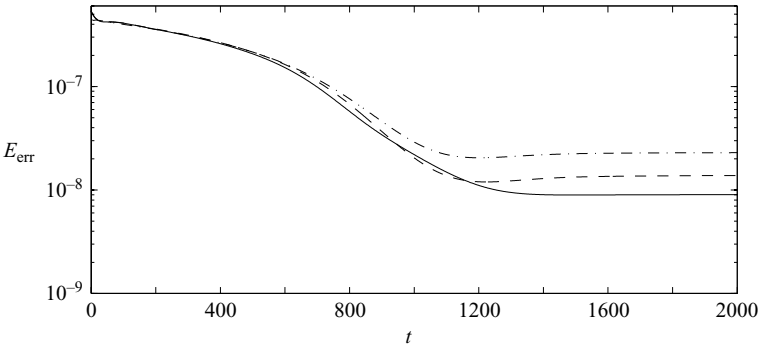

FIGURE 15. Comparison of the energy of the estimation error E_{err} for the streaky flow case for three different stochastic models. Solid: Correlated model with $d_y = 2.0$. Dashed: Correlated model with $d_y = 0.5$. Dash-dotted: uncorrelated.

6. Conclusions

Based on findings on how to improve the state estimation performance, reported in Hœpffner *et al.* (2005), combined with the state-feedback control used in, for instance, Bewley & Liu (1998) and Högberg & Henningson (2002), viscous instabilities, non-modal transient energy growth and inflectional instabilities in spatially developing boundary layer flows are controlled based on wall measurements.

The key to the improved performance of the estimator is the design of a relevant stochastic model for the external sources of disturbances. For this purpose we choose a correlation length. We also choose an amplitude distribution in wavenumber space such that it represents the most dominant wavenumbers in the specific flow being studied. This procedure leads to resolution-independent well-resolved estimation gains for the three measurements: streamwise and spanwise skin frictions and wall pressure. Both the sensor noise and the external disturbances are assumed to be white noise processes. As the estimator is switched on, there is an initial transient that propagates with the group velocity of the dominating disturbances through the computational domain. Upstream of this transient the estimate is converged. This feature makes the compensator control efficient since little extra time is needed to obtain a good state estimate where it is needed for control, i.e. above the actuation region.

This work has been partially financed by the Innovation fund at the Swedish Defence Research Agency (FOI) and from the EOARD grant FA8655-04-1-3032 which is greatfully acknowledged.

REFERENCES

ANDERSSON, P., BERGGREN, M. & HENNINGSON, D. S. 1999 Optimal disturbances and bypass transition in boundary layers. *Phys. Fluids* **11**, 134–150.

ANDERSSON, P., BRANDT, L., BOTTARO, A. & HENNINGSON, D. S. 2000 On the breakdown of boundary layer streaks. *J. Fluid Mech.* **428**, 29–60.

BERTOLOTTI, F. P., HERBERT, T. & SPALART, P. R. 1992 Linear and nonlinear stability of the Blasius boundary layer. *J. Fluid Mech.* **242**, 441–474.

BEWLEY, T. R. 2001 Flow control: new challenges for a new Renaissance. *Prog. Aerospace Sci.* **37**, 21–58.

BEWLEY, T. R. & LIU, S. 1998 Optimal and robust control and estimation of linear paths to transition. *J. Fluid Mech.* **365**, 305–349.

Butler, K. M. & Farrell, B. F. 1992 Three-dimensional optimal perturbations in viscous shear flow. *Phys. Fluids* A **4**, 1637–1650.

Cathalifaud, P. & Luchini, P. 2000 Algebraic growth in boundary layers: optimal control by blowing and suction at the wall. *Eur. J. Mech.* B - *Fluids* **19**, 469–490.

Chevalier, M., Hœpffner, J., Bewley, T. R. & Henningson, D. S. 2006 State estimation of wall bounded flow systems. Part 2. Turbulent flows. *J. Fluid Mech.* **552**, 167–187.

Cooke, J. C. 1950 The boundary layer of a class of infinite yawed cylinders. *Proc. Camb. Phil. Soc.* **46**, 645–648.

Herbert, T. 1997 Parabolized stability equations. *Annu. Rev. Fluid Mech.* **29**, 245–283.

Hœpffner, J., Chevalier, M., Bewley, T. R. & Henningson, D. S. 2005 State estimation in wall-bounded flow systems. Part 1. Laminar flows. *J. Fluid Mech.* **534**, 263–294.

Högberg, M., Bewley, T. R. & Henningson, D. S. 2003*a* Linear feedback control and estimation of transition in plane channel flow. *J. Fluid Mech.* **481**, 149–175.

Högberg, M., Bewley, T. R. & Henningson, D. S. 2003*b* Relaminarization of $\mathrm{Re}_\tau = 100$ turbulence using gain scheduling and linear state-feedback control. *Phys. Fluids* **15**, 3572–3575.

Högberg, M., Chevalier, M. & Henningson, D. S. 2003*c* Linear compensator control of a pointsource induced perturbation in a Falkner–Skan–Cooke boundary layer. *Phys. Fluids* **15**, 2449–2452.

Högberg, M. & Henningson, D. S. 1998 Secondary instability of cross-flow vortices in Falkner–Skan–Cooke boundary layers. *J. Fluid Mech.* **368**, 339–357.

Högberg, M. & Henningson, D. S. 2002 Linear optimal control applied to instabilities in spatially developing boundary layers. *J. Fluid Mech.* **470**, 151–179.

Kim, J. 2003 Control of turbulent boundary layers. *Phys. Fluids* **15**, 1093–1105.

Levin, O. 2003 Stability analysis and transition prediction of wall-bounded flows. Licentiate thesis, Royal Institute of Technology, Stockholm.

Lewis, F. L. & Syrmos, V. L. 1995 *Optimal Control*. Wiley-Interscience.

Luchini, P. 2000 Reynolds-number-independent instability of the boundary layer over a flat surface: optimal perturbations. *J. Fluid Mech.* **404**, 289–309.

Lundbladh, A., Berlin, S., Skote, M., Hildings, C., Choi, J., Kim, J. & Henningson, D. S. 1999 An efficient spectral method for simulations of incompressible flow over a flat plate. *Tech. Rep.* TRITA-MEK 1999:11. Department of Mechanics, Royal Institute of Technology, KTH.

Lundbladh, A., Henningson, D. S. & Johansson, A. 1992 An efficient spectral integration method for the solution of the Navier–Stokes equations. *Tech. Rep.* FFA TN 1992-28. The Aeronautical Research Institute of Sweden, FFA.

Malik, M. R., Zang, T. A. & Hussaini, M. Y. 1985 A spectral collocation method for the Navier–Stokes equations. *J. Comput. Phys.* **61**, 64–88.

Müller, B. & Bippes, H. 1988 Experimental study of instability modes in a three-dimensional boundary layer. *AGARD-CP* 438, 18.

Nordström, J., Nordin, N. & Henningson, D. S. 1999 The fringe region technique and the Fourier method used in the direct numerical simulation of spatially evolving viscous flows. *SIAM J. Sci. Comput.* **20**, 1365–1393.

Schlichting, H. 1979 *Boundary-Layer Theory*, 7th edn. Springer.

Schmid, P. J. & Henningson, D. S. 2001 *Stability and Transition in Shear Flows*. Applied Mathematical Sciences, vol. 142. Springer.

Yoshino, T., Suzuki, Y. & Kasagi, N. 2003 Evaluation of GA-based feedback control system for drag reduction in wall turbulence. In *Proc. 3rd Intl Symp. on Turbulence and Shear Flow Phenomena*, pp. 179–184.